

Cite this: *J. Mater. Chem. A*, 2022, 10, 4157

# A Li–In alloy anode and Nb<sub>2</sub>CT<sub>x</sub> artificial solid-electrolyte interphase for practical Li metal batteries†

Seung Hun Lee,  <sup>‡</sup>ab Mun Sek Kim,  <sup>‡</sup>c Jung-Hoon Lee,  <sup>d</sup> Ji-Hyun Ryu,  <sup>ab</sup> Vandung Do,  <sup>a</sup> Byeong Gwon Lee,  <sup>ab</sup> Woong Kim <sup>\*b</sup> and Won Il Cho  <sup>\*ab</sup>

Lithium metal (Li) has received growing attention for use in rechargeable electrochemical cells with various types of cathode owing to its potential as a high-capacity anode. However, continuous electrochemical reactions and uncontrolled electrodeposition at the surface of the anode hinder its practical usage. Here, through the coupling of a Li–In alloy as an anode material with Nb<sub>2</sub>CT<sub>x</sub> (an MXene) as an artificial solid-electrolyte interphase (Nb<sub>2</sub>CT<sub>x</sub> Li–In), we achieved a superior cycling performance to overcome the existing problems of Li anodes. The Li diffusion behavior and the interactions between the Nb<sub>2</sub>CT<sub>x</sub> Li–In alloy anode and Li were examined using density functional theory calculations, and it was confirmed that the Nb<sub>2</sub>CT<sub>x</sub> Li–In provides high Li affinities and controls Li migration. Then, the material characteristics of the Nb<sub>2</sub>CT<sub>x</sub> ASEI and Li–In alloy were respectively analyzed, and the Li electrodeposition behavior and improved reversibility were confirmed via various electrochemical experiments. The electrochemical performances of the Nb<sub>2</sub>CT<sub>x</sub> Li–In alloy anode were evaluated paired with a LiNi<sub>0.8</sub>Co<sub>0.1</sub>Mn<sub>0.1</sub>O<sub>2</sub> cathode (NCM811), and the capacity was stably maintained for >450 cycles. Finally, a Nb<sub>2</sub>CT<sub>x</sub> Li–In pouch cell (~272 W h kg<sup>-1</sup>, 500 W h L<sup>-1</sup>) was fabricated with a practical composition of high loading NCM811 (4.1 mA h cm<sup>-2</sup>) and a limited amount of electrolyte (2.4 μL (mA h)<sup>-1</sup>), and was operated for >200 cycles. The Nb<sub>2</sub>CT<sub>x</sub> Li–In alloy anodes exhibit a high reversibility and stability for Li deposition and migration during the repeated cycling of lithium metal batteries.

Received 1st November 2021  
Accepted 8th January 2022

DOI: 10.1039/d1ta09366e

rsc.li/materials-a

## 1. Introduction

Improving the energy density of rechargeable lithium (Li) batteries has become vital to meet the high energy storage requirements for the practical use of electrified vehicles and portable electronics.<sup>1,2</sup> Utilizing Li anodes for batteries is highly desirable to meet the high energy storage requirements, as Li has an ultrahigh theoretical specific capacity (3860 mA h g<sup>-1</sup> Li), a low electrochemical potential (−3.04 V vs. the standard hydrogen electrode), and a low density (0.534 g cm<sup>-3</sup>).<sup>3,4</sup> Furthermore, owing to the high compatibility of Li anodes with various lithiated/unlithiated cathode materials, the chemistries of high energy density batteries have been extensively studied to

surpass the theoretical energy density limit of conventional lithium-ion batteries (LIBs).<sup>1,5,6</sup>

Despite the aforementioned potential benefits of Li anodes, the high reactivity, uneven electro-deposition/dissolution of Li, and uncontrolled Li migration around the solid-electrolyte interphase (SEI) on the Li anode<sup>7,8</sup> during battery charge/discharge result in a low coulombic efficiency (CE) and a short cycle life for Li metal batteries (LMBs).<sup>9</sup> In particular, naturally formed SEIs are unstable because they are heterogeneous and prone to cracking during cycling due to the large volume changes taking place in the Li anode. This not only exposes the fresh Li surface, causing parasitic reactions with the electrolyte, but also aggravates the formation of dendritic and dead Li. The physicochemical characteristics of the substrate where Li is electrodeposited play an important role in regulating the behavior of Li electrodeposition and SEI formation.<sup>10,11</sup> Therefore, the design of a suitable Li deposition platform that enables stable and reversible electrochemical reactions during cycling has been considered important to ensure a sufficiently high LMB performance for practical applications.<sup>5,9</sup>

To date, diverse strategies have been studied to achieve a practical level of performance for LMBs.<sup>12,13</sup> Among them, Li alloys with Sn,<sup>14,15</sup> Au,<sup>16</sup> Mg,<sup>17</sup> B,<sup>18</sup> Al,<sup>19</sup> and In<sup>20,21</sup> for use as anode materials have been shown to allow improved

<sup>a</sup>Energy Storage Research Center, Korea Institute of Science and Technology (KIST), Seoul 02792, Republic of Korea. E-mail: wonic@kist.re.kr

<sup>b</sup>Department of Materials Science and Engineering, Korea University, Seoul 02841, Republic of Korea

<sup>c</sup>Department of Chemical Engineering, Stanford University, California 94305, USA

<sup>d</sup>Computational Science Research Center, Korea Institute of Science and Technology (KIST), Seoul 02792, Republic of Korea

† Electronic supplementary information (ESI) available. See DOI: 10.1039/d1ta09366e

‡ First author.

electrochemical reversibility and stability, favored Li adsorption and facilitated charge transfer kinetics. It has also been reported that Li alloy materials provide physicochemically stable Li hosts and improve the electrochemical properties of Li diffusion, nucleation, and growth on the anode surface.<sup>14,22</sup> Stable and functional Li deposition platforms, such as Li alloys and Li intermetallic compounds, can tolerate large volume changes during repeated Li electro-deposition/dissolution processes and prevent the parasitic reaction between fresh Li and the electrolyte at the surface of the Li anode.<sup>23,24</sup> Therefore, understanding the mechanism of Li alloy and Li intermetallic compounds for Li anodes provides several scientific benefits for the development of high-performance LMBs.<sup>20,25</sup>

In addition to the Li alloying strategy, the introduction of an artificial SEI (ASEI) layer has been considered as another promising approach to suppress dendrite formation and mitigate parasitic reactions.<sup>5,13,26</sup> A variety of ASEI materials have been reported to date, including those based on carbon,<sup>27,28</sup> polymers,<sup>29,30</sup> and transition metal.<sup>25,31</sup> For example, MXenes, a class of two-dimensional inorganic compounds, have attracted considerable attention as promising ASEIs owing to their high conductivity and layered structure and the high Li affinity of their surface functional groups, such as O and F atoms.<sup>32–35</sup> Among MXenes, Nb<sub>2</sub>CT<sub>x</sub> exhibits better electrochemical performance and reversibility than the most extensively studied MXene compounds such as Ti<sub>2</sub>CT<sub>x</sub> and Ti<sub>3</sub>C<sub>2</sub>T<sub>x</sub>.<sup>31,34,36</sup> However, these ASEI materials for anodes must overcome problems such as design and practical specific capacity of the anode, loading level of the cathode active material, amount of electrolyte, and battery operating conditions for commercial-level battery development.

Herein, we propose a lithium–indium (Li–In) alloy anode protected by an MXene-based (Nb<sub>2</sub>CT<sub>x</sub>) ASEI. This combination is illustrated in detail to elucidate the working mechanism of the Li–In alloy anode and the Nb<sub>2</sub>CT<sub>x</sub> ASEI. We investigated the Li affinity, Li migration, and electrochemical properties of the Li–In anode and Nb<sub>2</sub>CT<sub>x</sub> ASEI through computational science, physicochemical analysis, and electrochemical measurements. In addition, we demonstrate the practical use of a Li–In alloy that can be used as a substitute for conventional Li anodes. Furthermore, the influence of incorporating the Nb<sub>2</sub>CT<sub>x</sub> ASEI on top of the Li–In alloy anode is examined. Then, we proved the excellent reversibility and electrochemical properties of the Nb<sub>2</sub>CT<sub>x</sub> Li–In alloy anode by evaluating a full cell with high-loading LiNi<sub>0.8</sub>Mn<sub>0.1</sub>Co<sub>0.1</sub> (NMC811, 4.1 mA h cm<sup>-2</sup>). Finally, a pouch cell composed of the Nb<sub>2</sub>CT<sub>x</sub> Li–In alloy anode, an NCM811 cathode, and a limited amount of electrolyte is fabricated, and its electrochemical performance is evaluated.

## 2. Experimental

### 2.1 Li–In alloy fabrication

A Li–In foil was customized by Honjo Metal, Japan, and was supplied by KISCO Korea Co. Ltd. A Li–In ingot composed of 80 wt% high-purity Li (99.99%) and 20 wt% granular In powder ( $\phi$  2–3  $\mu$ m) was formed by direct mixing of the components at over 230 °C under an Ar atmosphere. Then, the ingot was cooled

to room temperature and subsequently roll-pressed to obtain 200  $\mu$ m-thick Li–In foil with a Cu current collector under an Ar atmosphere. The minimum thickness of Li–In foil with a uniform thickness and structure available from the company was 200  $\mu$ m.

### 2.2 Nb<sub>2</sub>CT<sub>x</sub> MXene synthesis

Nb<sub>2</sub>CT<sub>x</sub> MXene was prepared by etching Al from Nb<sub>2</sub>AlC with 50 wt% hydrofluoric acid (HF). 40 ml of 50 wt% HF (Sigma-Aldrich) was prepared in a Teflon beaker, and the prepared etchant was placed in an oil bath set at 40 °C.<sup>33</sup> With stirring, 2 g of Nb<sub>2</sub>AlC was slowly added to the etchant. The suspension was stirred for 4 days. After etching, the suspension was filtered by vacuum filtration and washed with deionized water by centrifugation until the pH value reached 6. After washing, the remaining Nb<sub>2</sub>CT<sub>x</sub> was dried in a vacuum oven at 50 °C overnight.

### 2.3 Fabrication of the Nb<sub>2</sub>CT<sub>x</sub> ASEI Li–In alloy anode

The Nb<sub>2</sub>CT<sub>x</sub> Langmuir–Blodgett ASEI (LBASEI) was fabricated by the Langmuir–Blodgett Scooping (LBS) process under ambient conditions.<sup>37</sup> For Nb<sub>2</sub>CT<sub>x</sub> LBASEI, the synthesized Nb<sub>2</sub>CT<sub>x</sub> particle was dispersed in pure ethanol (5 wt%), and it was sonicated for 30 min. The Nb<sub>2</sub>CT<sub>x</sub> LB film was prepared on the surface of water and scooped on a Cu substrate (5 cm by 8 cm). Then Nb<sub>2</sub>CT<sub>x</sub> on the Cu substrate was dried on a hot plate at 100 °C for 2 min. This process was repeated until the desired thickness of Nb<sub>2</sub>CT<sub>x</sub> LBASEI was obtained. Then it was transferred to a vacuum oven and kept overnight at 50 °C. Finally the Nb<sub>2</sub>CT<sub>x</sub> film was transferred onto Li–In electrodes (4 cm by 6 cm) from the Cu substrate by roll-pressing under a dry atmosphere at a dew point below –70 °C. The configuration of PP film|Cu|Nb<sub>2</sub>CT<sub>x</sub> LBASEI|Li–In|Cu|PP film was used for the roll-pressing. The distance between cylinder rolls is 80 to 90% of the thickness of the stacked component, and the rolling rate is 3.0 cm s<sup>-1</sup>. After transfer, the PP film and Cu substrate were removed and Nb<sub>2</sub>CT<sub>x</sub> Li–In was cut into disks ( $\phi$  14.8 mm) to fabricate coin cells. The thickness of Nb<sub>2</sub>CT<sub>x</sub> LBASEI was measured using an OLS4100 microscope (Olympus), a 3D-laser microscope, and its thickness ranged from 2.02 to 10.12  $\mu$ m.

### 2.4 DFT calculation

To elucidate the Li binding properties, we performed first-principles DFT calculations using a plane-wave basis and projector augmented-wave (PAW<sup>38,39</sup>) pseudopotentials with the Vienna *Ab initio* Simulation Package (VASP) code.<sup>40–43</sup> To include the effect of the van der Waals (vdW) dispersive interactions on binding energies, all structural relaxations with the revised vdW-DF2 functional<sup>44</sup> were implemented in VASP. 6  $\times$  6  $\times$  1, 3  $\times$  3  $\times$  3, and 3  $\times$  4  $\times$  1 *k*-point grids were used for the unit cells of Nb<sub>2</sub>CT<sub>x</sub>, the unit cell of Li<sub>13</sub>In<sub>3</sub>, and the (311) surface-orientated slab structure of Li<sub>13</sub>In<sub>3</sub>, respectively. And a 600 eV plane-wave was used for cut-off energy. Our PAW potentials explicitly treat thirteen valence electrons for Nb (4s<sup>2</sup>4p<sup>6</sup>4d<sup>4</sup>5<sup>1</sup>), three for In (5s<sup>2</sup>5p<sup>1</sup>), seven for F (2s<sup>2</sup>2p<sup>5</sup>), six for O (2s<sup>2</sup>2p<sup>4</sup>), four for C (2s<sup>2</sup>2p<sup>2</sup>), three for Li (1s<sup>2</sup>2s<sup>1</sup>), and one for H (1s<sup>1</sup>). Brillouin

zone integrations were performed with a Gaussian smearing of 0.05 eV.<sup>45</sup> The initial structure of the Li<sub>13</sub>-In<sub>3</sub> alloy is obtained from a previous experiment.<sup>46</sup> To compute the Li binding energy on Nb<sub>2</sub>CT<sub>x</sub>, we only relaxed the Li atom and terminal groups while fixing the Nb<sub>2</sub>CT<sub>x</sub> layer with a 20 Å vacuum layer. For the Li adsorption on the (311) surface of Li<sub>13</sub>-In<sub>3</sub>, we relax adsorbed the Li atom along the *c*-axis while fixing the Li<sub>13</sub>In<sub>3</sub> slab geometry and the in-plane direction of the adsorbed Li atom on the slab with a 20 Å vacuum layer. The ions were relaxed until the Hellmann-Feynman forces were less than 0.01 eV per Å. On-site Hubbard Coulomb (*U*) and Hund's exchange (*J*) parameters of 2.8 eV and 1.4 eV for the Nb 4d state were chosen following previous studies for 4d transition metals.<sup>47</sup>

To compute the binding energies of Li on the Nb<sub>2</sub>CT<sub>x</sub> and Li<sub>13</sub>In<sub>3</sub> surfaces, three sets of calculations were performed for each functional considered. First, we optimized the slab prior to Li adsorption ( $E_{\text{slab}}$ ); we then optimized and computed an atomic reference energy ( $E_{\text{Li-atom}}$ ) for Li within a 20 Å × 20 Å × 20 Å cubic supercell; and finally, we relaxed the Nb<sub>2</sub>CT<sub>x</sub> and Li<sub>13</sub>-In<sub>3</sub> slabs with adsorbed Li ( $E_{\text{Li-atom/slab}}$ ). The binding energies were obtained from the difference

$$E_{\text{B}} = E_{\text{Li-atom/slab}} - (E_{\text{slab}} + E_{\text{Li-atom}})$$

For the nudged elastic band (NEB) simulations, we used the VTST extension of the VASP code with the climbing-image technique.<sup>48,49</sup> We sampled a Li diffusion path on Nb<sub>2</sub>C-O with seven images. The forces on the images were optimized until they were less than 0.01 eV per Å.

## 2.5 Material characterization tools and method

The X-ray diffraction (XRD, Rigaku, D/MAX-2500/PC diffractometer, Cu K $\alpha$ 1) patterns were obtained with a scan step of 0.02° with 1 s per step to compare the crystal structure of the Nb<sub>2</sub>AlC MAX phase, synthesized Nb<sub>2</sub>CT<sub>x</sub> MXene, Li, and Li-In alloy. The Li and Li-In alloy were covered with Kapton tape under a dry atmosphere below a dew point of -70 °C to prepare the XRD samples.

A scanning electron microscope (SEM, Inspec F50) was used to obtain high-magnification images of the materials and anode.

X-ray photoelectron spectroscopy (XPS, PHI 5000 VersaProbe (Ulvac-PHI), background pressure of 2.0 × 10<sup>-7</sup> Pa, source of monochromator Al K $\alpha$  (1486.6 eV), anode (24.5 W, 15 kV), spot size of 100 μm × 100 μm) was used to evaluate the chemical properties of the binding species.

Cycled electrode surface morphologies were investigated using focused ion beam (FIB) microscopy (Quanta 3D FEG, FEI). Cycled cells were opened using a coin cell disassembler, and anodes were cleaned with dimethyl carbonate (DMC) to wash the remaining electrolyte and dried in a vacuum oven at 50 °C. Anodes were transported from the glovebox to the FIB equipment, and a voltage of 5 kV was applied to obtain FIB images of the Li anode. And ion beam currents of 7 nA to 0.5 nA were used for sample milling to observe the cross-sectional image of the cycled anode.

## 2.6 Electrochemical analysis

A 2032 coin cell kit (Wellcos, Japan) was used for electrochemical measurements. 200 μm of Li and Li-In foil (Honjo Metal, Japan, supplied by KISCO Korea) was used as the anode and substrate for the Nb<sub>2</sub>CT<sub>x</sub> ASEI film. Anodes were fabricated by punching it into circular disks ( $\phi$  14.8 mm). A 4.1 mA h cm<sup>-2</sup> NCM (8/1/1) cathode (LiNi<sub>0.8</sub>Co<sub>0.1</sub>Mn<sub>0.1</sub>O<sub>2</sub>, supplied by LG Energy Solution) was punched into circular disks ( $\phi$  12 mm) and used for fabricating a full cell. An 11 μm thick polyethylene separator (W-Scope, Korea) punched into circular disks ( $\phi$  18 mm) was used for all coin cells. And 40 μL of electrolyte was used (20 μL for the anode side and 20 μL for the cathode side, 8.6 μL (mA h)<sup>-1</sup>).

The formulation of the electrolyte used for electrochemical measurements is as follows: 0.6 M lithium bis(trifluoromethanesulfonyl)imide (LiTFSI, Sigma Aldrich), 0.4 M lithium bis(oxalato)borate (LiBOB, Sigma Aldrich), 0.4 M lithium fluoride (LiF, Sigma Aldrich), 0.1 M lithium nitrate (LiNO<sub>3</sub>, Alfa Aesar), 0.05 M lithium hexafluorophosphate (LiPF<sub>6</sub>, PanaX Etech), 0.03 M lithium tetrafluoroborate (LiBF<sub>4</sub>, Sigma Aldrich) in ethylene carbonate (EC, PanaX Etech) : DMC (PanaX Etech) in a 4 : 6 weight ratio with 1 wt% fluoroethylene carbonate (FEC, PanaX Etech) & 3 wt% di-2,2,2-trifluoroethyl carbonate (TFEC, TCI Tokyo Chemical). The salts were dissolved in EC : DMC solvent first and stirred for 24 h. Then the solution was sonicated for 10 minutes and the solvent additives were added.

Asymmetric coin cells were fabricated for the nucleation overpotential measurement. Pristine Cu foil and Nb<sub>2</sub>CT<sub>x</sub> LBA-SEI on Cu foil prepared *via* the LBS method were punched into circular disks ( $\phi$  18 mm) and used as the reference electrode. The counter electrode was 200 μm thick Li-In (Honjo Metal, Japan, supplied by KISCO Korea) with Nb<sub>2</sub>CT<sub>x</sub> LBASEI ( $\phi$  14.8 mm). A current density of 0.05 mA cm<sup>-2</sup> was applied to obtain the voltage profiles for calculating the nucleation overpotential value using a galvanostatic potentiostat (Biologics VSP/VMP3).

Li|Li, Li-In|Li-In and Li-In Nb<sub>2</sub>CT<sub>x</sub>|Nb<sub>2</sub>CT<sub>x</sub> Li-In symmetric coin cells were used to measure the practical areal capacity and Li stripping/plating performance. A disk size of  $\phi$  14.8 mm was used for the electrodes. For practical areal capacity measurement, galvanostatic conditions were applied with a current density of 4 mA cm<sup>-2</sup> and a voltage cut-off of 1.0 V. For stripping/plating, galvanostatic conditions were applied with a current density and capacity of 1 mA cm<sup>-2</sup>/1 mA h cm<sup>-2</sup> and 2 mA cm<sup>-2</sup>/2 mA h cm<sup>-2</sup> using a battery cycler (Maccor Series 4000).

For the cycling performance, NCM811|Li, NCM811|Li-In, NCM811|Nb<sub>2</sub>CT<sub>x</sub> Li and NCM811|Nb<sub>2</sub>CT<sub>x</sub> Li-In full cells (coin cells) were used. The NCM811 single-sided cathode (LG Chem., Korea) has an areal capacity of 4.1 mA h cm<sup>-2</sup> and loading of 21.6 mg cm<sup>-2</sup>. Cycling was performed with the first cycle at 0.1C charging and discharging as the formation step, and each cycle is repeated at 0.5C charging and 1C discharging rates or 0.3C charging and 1C discharging rates using a battery cycler (Maccor Series 4000). The charging steps consisted of constant current charging to 4.3 V and constant voltage charging with

a cut-off current value of 0.05C. The voltage window was set to 2.7–4.3 V.

For the pouch cell fabrication, the configuration of Cu|Nb<sub>2</sub>CT<sub>x</sub> Li-In|NCM811|Al|NCM811|Nb<sub>2</sub>CT<sub>x</sub> Li-In|Cu was used to construct a 57.4 mA h battery. We used two 2 cm by 3.5 cm single sided Nb<sub>2</sub>CT<sub>x</sub> Li-In alloy anodes, a 2 cm by 3.5 cm double-sided cathode, two 2 cm by 3.5 cm PE separators, and 150 μL of electrolyte. The pouch cell was tested with 0.1C charging and discharging for the 1<sup>st</sup> formation cycle and 0.1C charging and 0.5C discharging for cycling. The charging steps consisted of constant current charging to 4.3 V and constant voltage charging with a cut-off current value of 0.05C. The voltage window was set to 2.7 V to 4.3 V. For gravimetric and volumetric energy density calculation, the following values were used: Nb<sub>2</sub>CT<sub>x</sub> Li-In (39.63 mA h cm<sup>-2</sup> (areal capacity), 13.52 mg cm<sup>-2</sup> (areal weight), and 201.02 μm (thickness)), NCM811 (8.2 mA h cm<sup>-2</sup> (areal capacity), 22.48 mg cm<sup>-2</sup> (areal weight), and 68 μm (thickness)), electrolyte (2.4 μL (mA h)<sup>-1</sup> (normalized amount), 140 μL (total amount), and 1.17 mg μL<sup>-1</sup> (density)), Cu current collector (7.168 mg cm<sup>-2</sup> (areal weight) and 8 μm (thickness)), Al current collector (3.24 mg cm<sup>-2</sup> (areal weight) and 12 μm (thickness)), PE separator (0.45 mg cm<sup>-2</sup> (areal weight) and 11 μm (thickness)), and a reaction potential of 3.8 V.

All long-term electrochemical analyses were performed at ~26 °C using a low-temp. incubator (IL3-25, Lab Companion).

Also, full cells were used for cyclic voltammetry (CV) performed in the 2.7 V to 4.3 V voltage range at a scan rate of 0.1 mV s<sup>-1</sup>, and electrochemical impedance spectroscopy (EIS) was performed in the 0.03 Hz to 500 kHz frequency range using a galvanostatic potentiostat (Biologics VSP/VMP3).

### 3. Results and discussion

#### 3.1 Investigation of the Li-In alloy anode

The Li-In alloy anode was investigated to understand the components of the Li-In species and the characteristics of Li migration on the alloyed anode. The Li-In alloy anode was designed with consideration of the practical gravimetric and volumetric capacities and the distribution of the Li-In species. With the aim of replacing conventional Li metal, the designed ratio of Li to In was set to 80 : 20 wt%. The theoretical composition was calculated using the Li-In phase diagram shown in Fig. S1a,<sup>†</sup> and this specific composition allowed for an appropriate manufacturing process and an acceptable capacity that satisfied the large-scale production and practical requirements for LMBs. Based on this ratio, the thinnest Li-In alloy anode that could be uniformly processed was 200 μm. Additional roll-pressing cycles were conducted for preparing thinner Li-In anodes (Fig. S15 and Table S2<sup>†</sup>). However, anodes with uniform thickness and structure were used for achieving a precise n/p ratio and experimental reproducibility. The Li-In anode consisted of two phases, Li and Li<sub>13</sub>In<sub>3</sub>, and Li : Li<sub>13</sub>In<sub>3</sub> was calculated to be 74.68 : 25.32 wt%.

Fig. 1a shows the X-ray diffraction (XRD) pattern of the Li-In alloy anode, which reveals that the anode is composed of Li and Li<sub>13</sub>In<sub>3</sub>, with the dominant crystal plane being (311) Li<sub>13</sub>In<sub>3</sub>. To

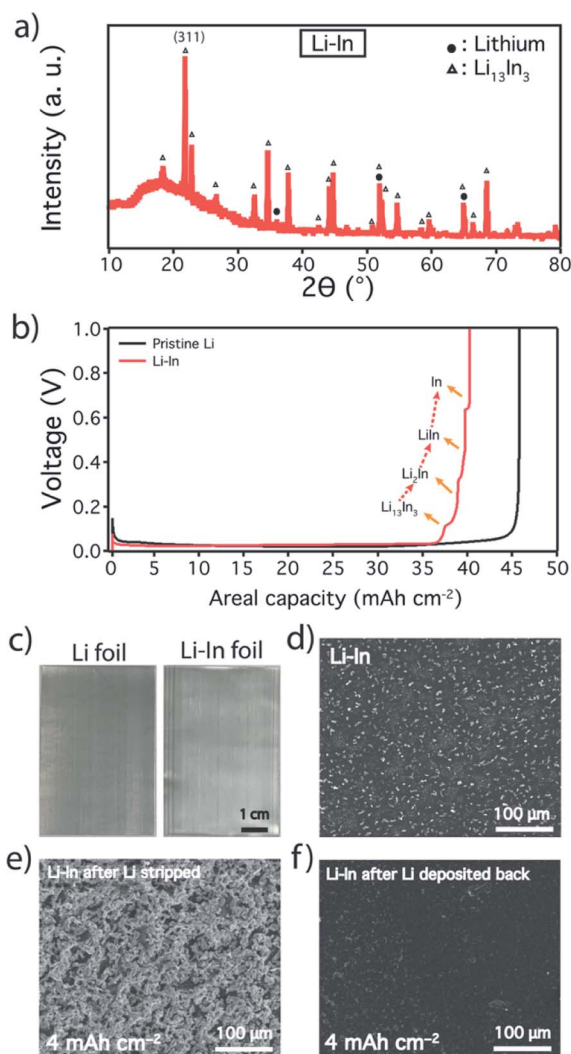


Fig. 1 Material characterization of the Li-In alloy anode. (a) XRD pattern of the pristine Li-In alloy anode. (b) Practical areal capacity measurements for the Li and Li-In alloy anodes. The areal masses of the Li and Li-In alloy anodes are 12.28 and 13.24 mg cm<sup>-2</sup>, respectively. (c) Optical images of the Li foil (left) and the Li-In foil (right). (d) SEM image of the pristine Li-In alloy anode. The bright spots are the Li<sub>13</sub>In<sub>3</sub> intermetallic compound, and the dark background is Li. SEM surface morphology images of the Li-In alloy anode after galvanostatic (e) stripping and (f) replating of Li with a symmetric cell (Li-In|Li-In) at a current density of 1 mA cm<sup>-2</sup> and for a capacity of 4 mA h cm<sup>-2</sup>.

assess the crystal patterns after the electrochemical reactions of the Li-In alloy electrodes, XRD measurements were carried out after 4 mA h cm<sup>-2</sup> Li stripping and deposition using a Li-In|Li-In symmetric cell (Fig. S2<sup>†</sup>). A capacity of 4 mA h cm<sup>-2</sup> was set to match the NCM811 cathode used in the full cell, which is discussed later in detail. With this capacity, the XRD patterns shown in Fig. S2a and b<sup>†</sup> confirm that Li<sub>13</sub>In<sub>3</sub> retains its composition, indicating that this phase does not participate in electrochemical reactions within the selected capacity. To determine the practical capacity and possible phase transition of the Li-In alloy anode, Li was fully stripped to 37.5 mA h cm<sup>-2</sup> until no Li peaks were detected (Fig. S2c–f<sup>†</sup>). Beyond this point, a phase transition was observed from Li<sub>13</sub>In<sub>3</sub> to Li<sub>2</sub>In, LiIn, and In.

The capacity and phase transition of the Li–In alloy anode were closely observed using symmetric cells (Fig. 1b). The practical areal capacities of the 200  $\mu\text{m}$  Li and Li–In alloy anodes were found to be 45.53  $\text{mA h cm}^{-2}$  (3707.96  $\text{mA h g}^{-1}$ ) and 39.97  $\text{mA h cm}^{-2}$  (3021.44  $\text{mA h g}^{-1}$ ), respectively. The practical capacity of the Li–In alloy anode was  $\sim 88\%$  that of the Li anode. Later in the paper, we confirm that although the practical capacity of the Li–In anode is  $\sim 12\%$  lower than that of the Li anode, the Li–In anode exhibited higher electrochemical reversibility, indicating that the reduction in the practical capacity can be compensated for with the improved electrochemical stability. For the phase transition of the alloy anode, phase transition plateaus observed in the 35–40  $\text{mA h cm}^{-2}$  range were observed at 0.12, 0.31, and 0.64 V (Fig. 1b), which are consistent with previously reported values.<sup>50,51</sup> The total capacity measured from the phase transition was approximately 2.3  $\text{mA h cm}^{-2}$ , which is 5.75% that of the practical areal capacity of the Li–In alloy anode, indicating only a fractional capacity contribution from the  $\text{Li}_{13}\text{In}_3$  species.

To physically observe the fabricated Li–In alloy anode, optical and scanning electron microscopy (SEM) images of the Li and Li–In alloy anodes were compared, as shown in Fig. 1c–f. More specifically, as shown in Fig. 1d, the  $\text{Li}_{13}\text{In}_3$  intermetallic compounds (bright regions) were evenly distributed. The surface morphology of the 4  $\text{mA h cm}^{-2}$  Li-stripped Li–In alloy anode was also observed by SEM (Fig. 1e) to examine the skeleton of  $\text{Li}_{13}\text{In}_3$ . The enlarged backscattered electron (BSE) image of the 4  $\text{mA h cm}^{-2}$  Li-stripped Li–In alloy anode and the corresponding energy dispersive X-ray spectroscopy (EDX) mapping image of In are shown in Fig. S3a and b.† In addition, the phase diagram (Fig. S1†) and XRD data (Fig. S2a†) were obtained to assess the morphology of the distributed compounds, wherein the bright regions observed in Fig. 1d–f were attributed to the  $\text{Li}_{13}\text{In}_3$  intermetallic compounds. Furthermore, focused ion beam (FIB) milling was used to obtain a cross-sectional image of  $\text{Li}_{13}\text{In}_3$  (Fig. S3c†). Overall, a highly porous  $\text{Li}_{13}\text{In}_3$  skeleton was observed for the Li–In alloy anode; later, we demonstrate that the  $\text{Li}_{13}\text{In}_3$  skeleton allows uniform Li electrodeposition. The surface morphology of the Li–In alloy anode after the redeposition of Li is shown in Fig. 1f, wherein uniform Li electrodeposition can be observed without prominent Li dendrites. These results confirm that the Li–In alloy anode is suitable for use in LMBs.

### 3.2 DFT analyses of the Li–In alloy anode

van der Waals (vdW)-corrected density functional theory (DFT) calculations were then performed to understand the adsorption behavior of Li on the  $\text{Li}_{13}\text{In}_3$  surface. As the  $\text{Li}_{13}\text{In}_3$  (311) surface was the most dominant crystal plane in  $\text{Li}_{13}\text{In}_3$  (Fig. 1a), the Li adatom adsorption energy and diffusion barriers were calculated based on the  $\text{Li}_{13}\text{In}_3$  (311) surface. It has been found that the binding energies of Li, the  $\text{Li}_2$  clusters, and the  $\text{Li}_3$  clusters on the Li (110) surface were  $-1.40$ ,  $-2.75$ , and  $-1.68$  eV, respectively.<sup>25,27</sup> This binding energy trend suggests that Li is likely to form localized Li aggregates that induce the formation of Li dendrites and rougher Li electrodeposits. To relatively

compare these binding energies of Li on the Li (110) surface with those on the  $\text{Li}_{13}\text{In}_3$  (311) surface, the Li binding energies were calculated using the  $\text{Li}_{13}\text{In}_3$  (311) surface-oriented unit cell with the lattice parameters of the optimized unit cell, *i.e.*,  $a = 16.26$  Å,  $b = 9.39$  Å,  $c = 16.26$  Å,  $\alpha = 90^\circ$ ,  $\beta = 80.41^\circ$ , and  $\gamma = 106.78^\circ$  (Fig. 2a). Fig. 2b shows the computed Li binding energies for  $18 \times 11$  grid points on the  $\text{Li}_{13}\text{In}_3$  (311) surface, as represented by a contour map. The binding energy for each point was calculated by relaxing only the out-of-plane direction of the Li atoms. As the color progresses from green to dark blue, the Li binding energy becomes more stable. According to the DFT calculations, the Li binding energies near the In atoms (orange points in Fig. 2b) tend to be more stable than those near the Li atoms. The most stable binding energy of Li on the  $\text{Li}_{13}\text{In}_3$  (311) surface is  $-1.936$  eV, which is more stable than that ( $-1.411$  eV) of Li on the Li (110) surface by  $\sim 0.5$  eV (Fig. 2c). This indicates that Li is adsorbed more strongly on the  $\text{Li}_{13}\text{In}_3$  (311) surface than on the Li (110) surface. Moreover, it supports the fact that the  $\text{Li}_{13}\text{In}_3$  (311) surface allows stable electrodeposition for the first adsorbed Li species. The binding energies of the second and third adsorbed Li on the  $\text{Li}_{13}\text{In}_3$  (311) surface were  $-1.712$  and  $-1.794$  eV, respectively, confirming that the uniform adsorption of Li on the  $\text{Li}_{13}\text{In}_3$  (311) surface is thermodynamically more stable than that on the Li (110) surface.

The diffusion barriers of Li across the  $\text{Li}_{13}\text{In}_3$  (311) surface were then calculated to understand the surface diffusion characteristics of Li in Li–In alloy anodes. The two major energetically favorable diffusion pathways between the two most stable Li-binding sites are shown in Fig. S4.† In addition, Fig. 2d shows a comparison of the diffusion barriers of the two pathways (denoted as  $\text{Li}_{13}\text{In}_3^*$  and  $\text{Li}_{13}\text{In}_3^{**}$ ) on the  $\text{Li}_{13}\text{In}_3$  (311) surface, along with that on the Li (110) surface, while the relative energy profiles for the two probable Li diffusion pathways are shown in Fig. 2e. Furthermore, Li adatom diffusion on the  $\text{Li}_{13}\text{In}_3$  (311) surface is illustrated in Fig. S4.† In the profiles of the diffusion pathways, the two end points represent the most stable Li adsorption sites on the  $\text{Li}_{13}\text{In}_3$  (311) surface, which were marked as 0.00 eV for reference. The triangular points indicate the local minima of the various diffusion pathways. The calculated diffusion barriers of  $\text{Li}_{13}\text{In}_3^*$  (orange) and  $\text{Li}_{13}\text{In}_3^{**}$  (brown) were 0.759 eV and 0.971 eV, respectively, which are much higher than that on the Li (110) surface (0.025 eV). This means that Li spontaneously diffuses after the reduction of the Li-ion on the Li (110) surface and then aggregates to promote the dendritic formation of Li.<sup>25</sup> It has been found that the high diffusion barrier of Li is beneficial to the high surface area Li electrodeposition substrates as the high diffusion barrier of Li helps to minimize localized Li adatom migration.<sup>25</sup> As the morphology of the  $\text{Li}_{13}\text{In}_3$  skeleton (Fig. 1e) exhibited a large surface area, the high binding energy and diffusion barrier of Li for the  $\text{Li}_{13}\text{In}_3$  (311) surface (Fig. 2d) explain the uniform and smoothed Li electrodeposition obtained in Fig. 1e.

It has also been found that the high diffusion barrier of Li is beneficial to the high surface area of Li electrodeposition substrates, as this high diffusion barrier helps to minimize localized Li adatom migration.<sup>25</sup> As the  $\text{Li}_{13}\text{In}_3$  skeleton (Fig. 1e) exhibits a large surface area, the high binding energy and high

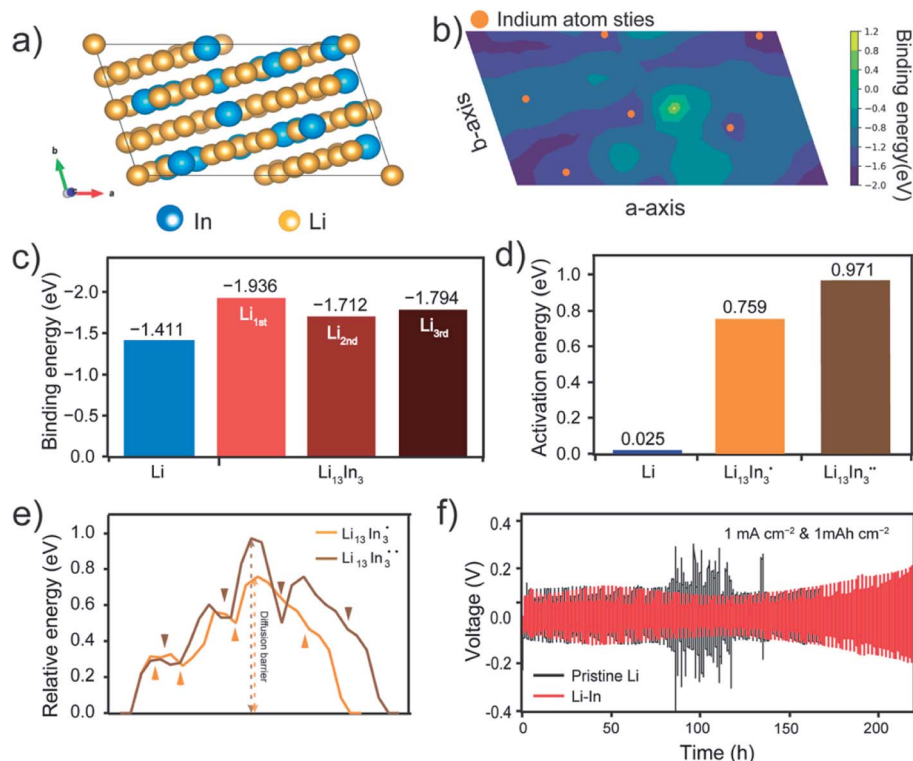


**Fig. 2** DFT calculations for the Li–In alloy anode. (a) The atomic arrangements of Li (yellow) and In (blue) as viewed in the (311) surface of the  $\text{Li}_{13}\text{In}_3$  unit cell. (b) Li binding energy on the (311) surface of  $\text{Li}_{13}\text{In}_3$ . Orange spots correspond to the In atom sites close to the (311) surface. (c) Li binding energy of the first adsorbed Li on the Li (110) surface at the most stable site. Li binding energies of the first, second, and third adsorbed Li on the  $\text{Li}_{13}\text{In}_3$  (311) surface at the most stable site. (d) Li activation energy for surface diffusion on the Li (110) and  $\text{Li}_{13}\text{In}_3$  (311) surfaces for two stable pathways ( $\text{Li}_{13}\text{In}_3^*$  and  $\text{Li}_{13}\text{In}_3^{**}$ ). The two diffusion paths start at the most stable position on the  $\text{Li}_{13}\text{In}_3$  (311) unit surface and reach the same point along energetically advantageous positions. (e) Diffusion barriers and relative energy changes according to the paths of  $\text{Li}_{13}\text{In}_3^*$  (orange) and  $\text{Li}_{13}\text{In}_3^{**}$  (brown), respectively. The small triangles in the graph represent the local energy minima present in each diffusion pathway. (f) Galvanostatic Li stripping/plating voltage profile for pristine Li (black) and Li–In (red). Voltage profiles were measured using a Li|Li and Li–In|Li–In symmetric cell at a fixed current density of  $1 \text{ mA cm}^{-2}$  and a capacity of  $1 \text{ mA h cm}^{-2}$ .

diffusion barrier of Li for the  $\text{Li}_{13}\text{In}_3$  (311) surface (Fig. 2d) account for the uniform and smooth Li electrodeposition shown in Fig. 1f.

Galvanostatic stripping/plating cycling was further conducted to investigate the reversibility of the Li electrodeposition/stripping cycles of the Li–In alloy anode. The voltage profiles of the Li (black) and Li–In alloy anodes (red) collected from Li|Li and Li–In|Li–In symmetric cells are compared in Fig. 2f. As shown, the voltage profile of Li exhibits a sudden voltage spike after 100 h, which is caused by the large overpotential driven by the build-up of SEIs and/or depletion of the electrolyte. In contrast, the voltage profile of Li–In exhibited a reduced overpotential and a prolonged reversibility of Li electrodeposition/stripping cycles over >200 h, thereby demonstrating the superior electrochemical reversibility of the Li–In alloy anode compared to the Li anode.

### 3.3 Characterization of the structure and adatom binding of $\text{Nb}_2\text{CT}_x$ MXene

$\text{Nb}_2\text{CT}_x$  (an MXene) was successfully prepared from  $\text{Nb}_2\text{AlC}$  (MAX phase) and was applied as an ASEI to further enhance the electrochemical performance and protect the Li–In alloy anode.

Although the Li–In anode has high Li affinity, the porous  $\text{Li}_{13}\text{In}_3$  structure (Fig. 1e), revealed during the Li plating/stripping process, can induce physical and electrical non-uniformity on the anode surface. The  $\text{Nb}_2\text{CT}_x$  ASEI was applied to prevent this non-uniformity. This study focused on  $\text{Nb}_2\text{CT}_x$  as an ASEI because it has a high binding energy for Li, high Li-ion conductivity, and a low surface diffusion barrier for Li, and exhibits a quasi-hosting feature for Li.<sup>51,52</sup> In addition, these properties are reported to be superior to those of  $\text{Ti}_2\text{CT}_x$  or  $\text{Ti}_3\text{C}_2\text{T}_x$ , which are the most commonly studied MXene materials.<sup>33,36</sup> To verify the synthesis of  $\text{Nb}_2\text{CT}_x$  from  $\text{Nb}_2\text{AlC}$ , SEM images were obtained, as shown in Fig. 3a and b, where the  $\text{Nb}_2\text{AlC}$  particles and layered structure of the etched  $\text{Nb}_2\text{CT}_x$  can be observed. EDX elemental mapping analysis (Fig. S5†) was carried out on  $\text{Nb}_2\text{CT}_x$  and  $\text{Nb}_2\text{AlC}$ , wherein distinct differences were observed in the Al, F and O peaks. More specifically, the Al peak in  $\text{Nb}_2\text{CT}_x$  is absent and F and O peaks are clearly present compared to the case of  $\text{Nb}_2\text{AlC}$ . It should be noted here that the O content originates from the termination functional group ( $\text{T}_x$ ) of  $\text{Nb}_2\text{CT}_x$  and surface oxidation layer.<sup>53</sup>

The key structural difference between the MAX phase and MXene is that MXene possesses a two-dimensional (2D) layered

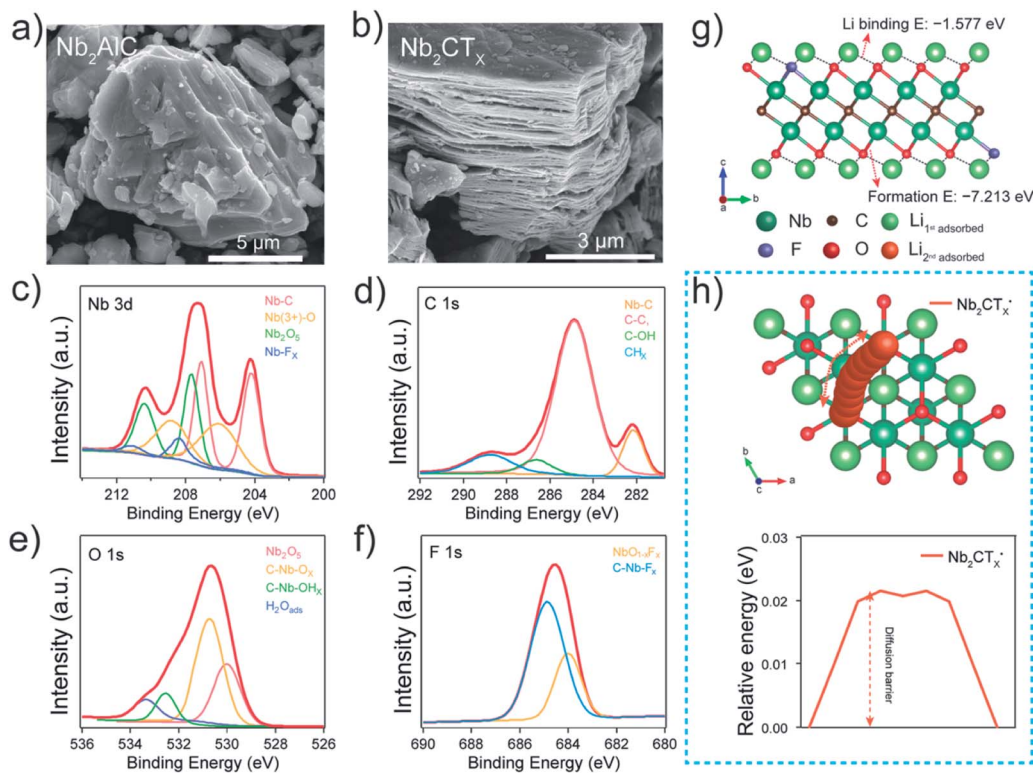


Fig. 3 Material characterization and DFT calculations of  $\text{Nb}_2\text{CT}_x$  MXene for the LBASEI. SEM images of (a)  $\text{Nb}_2\text{AlC}$  and (b)  $\text{Nb}_2\text{CT}_x$ . High resolution deconvoluted XPS spectra of  $\text{Nb}_2\text{CT}_x$  (c) Nb 3d, (d) C 1s, (e) O 1s, and (f) F 1s. (g)  $\text{Nb}_2\text{CT}_x$  atomic structure with termination groups and Li adatoms. The cyan blue, purple, brown, red, green, and orange spheres represent Nb, F, C, O, first adsorbed Li, and second adsorbed Li, respectively. The formation energy of  $-\text{O}-$  which is the major termination group on the  $\text{Nb}_2\text{C}$  surface is  $-7.213$  eV and the binding energy for the first adsorbed Li is  $-1.577$  eV. (h) Atomic structure of the diffusion pathway of the second adsorbed Li on the surface of  $\text{Nb}_2\text{C}-\text{O}-\text{Li}$  (top, orange) and the relative energy change according to  $\text{Nb}_2\text{C}-\text{O}-\text{Li}^*$  (bottom).

structure. In the XRD pattern of  $\text{Nb}_2\text{CT}_x$  shown in Fig. S6,<sup>†</sup> the (103) peak from the MAX phase disappeared, indicating the removal of the Al layer, while the (002) peak of  $\text{Nb}_2\text{AlC}$  was shifted to a lower angle after synthesis.<sup>54</sup> The removed Al layer and increased interlayer spacing of  $\text{Nb}_2\text{CT}_x$  thereby indicate that the structure of the bulk  $\text{Nb}_2\text{AlC}$  changed to the layered structure of  $\text{Nb}_2\text{CT}_x$  after treatment.

Subsequently, X-ray photoelectron spectroscopy (XPS) was performed to further understand the surface chemistry of  $\text{Nb}_2\text{CT}_x$ , including the termination functional groups. The high-resolution Nb 3d, C 1s, O 1s, and F 1s (Fig. 3c–f) spectra were analyzed for  $\text{Nb}_2\text{CT}_x$ , and the presence of a  $\text{Nb}_2\text{O}_5$  surface oxidation layer as well as  $-\text{O}-$  and  $-\text{F}$  termination groups. The deconvoluted Nb 3d peaks consist of Nb–C,  $\text{Nb}^{3+}-\text{O}$ ,  $\text{Nb}_2\text{O}_5$ , and Nb– $\text{F}_x$  with binding energies of 204.0, 205.7, 207.3, and 208.2 eV, respectively.<sup>55,56</sup> The Nb–C signal corresponds to the interior bond of  $\text{Nb}_2\text{C}$ , while the  $\text{Nb}_2\text{O}_5$  signal represents the exterior surface oxidation layer. The  $\text{Nb}^{3+}-\text{O}$  and Nb– $\text{F}_x$  peaks correspond to the  $-\text{O}-$  and  $-\text{F}$  termination groups on the  $\text{Nb}_2\text{CT}_x$  surface, which were also detected for C–Nb– $\text{O}_x$  (530.6 eV) and  $\text{NbO}_{1-x}-\text{F}_x$  (684.0 eV), as shown in their O 1s and F 1s spectra, respectively.<sup>55</sup> A wide scan of the XPS spectra is presented in Fig. S7a,<sup>†</sup> wherein the disappearance of the Al layer after etching was confirmed (Fig. S7b<sup>†</sup>).

To understand the Li adsorption behavior on  $\text{NbCT}_x$ , we have calculated the formation energies and Li binding energies of  $\text{Nb}_2\text{CT}_x$  for different termination groups using vdW-corrected DFT calculations. The schematic shown in Fig. 3g represents the atomic arrangement of the  $\text{Nb}_2\text{C}$  surface with termination groups where Li atoms are adsorbed. The  $-\text{O}-$  surface termination group on the  $\text{Nb}_2\text{C}$  surface is known to be the most suitable adsorption site for Li.<sup>35,57</sup> The DFT calculations also show that the  $-\text{O}-$  termination group is likely to form and has the most stable formation energy ( $-7.213$  eV) and Li binding energy ( $-1.577$  eV) compared to the other cases (see Table S1<sup>†</sup>). Moreover, the Li binding energy to the oxygen termination group ( $\text{Nb}_2\text{C}-\text{O}-$ ) is more stable than the Li binding energy to the Li (110) surface ( $-1.411$  eV). Stable Li binding energy facilitate the wetting of Li electrodeposition more favourably compared to the Li surface without  $\text{Nb}_2\text{CT}_x$ .

We then investigated the 2<sup>nd</sup> adsorbed Li diffusion behaviour on the  $\text{Nb}_2\text{CT}_x$  ASEI layer. To do this, the pathway and barrier of the 2<sup>nd</sup> adsorbed Li diffusion on the  $\text{Nb}_2\text{C}-\text{O}-\text{Li}$  surface (Fig. 3g, h) were calculated using NEB calculations. The  $\text{Nb}_2\text{C}-\text{O}-\text{Li}$  is chosen because the  $-\text{O}-$  is a major termination group<sup>53</sup> for  $\text{Nb}_2\text{CT}_x$ . The series of orange circles shown in Fig. 3h represent the diffusion pathway of the 2<sup>nd</sup> adsorbed Li between the most stable sites on the  $\text{Nb}_2\text{C}-\text{O}-\text{Li}$  surface. The energy of

the diffusion barrier was calculated to be 0.021 eV (Fig. 3h), which is smaller than that of Li diffusion on the Li (110) surface (0.025 eV). In addition, the Nb<sub>2</sub>CT<sub>x</sub> ASEI spontaneously gets lithiated upon direct contact with the Li–In alloy anode (Fig. S8b†). The right-hand image in Fig. S8b† shows the Nb<sub>2</sub>CT<sub>x</sub> Li–In anode after 3 days in a dry atmosphere below a dew point of –70 °C. The color change from gray to dark brown is attributed to spontaneous lithiation. These simulation results indicate that the presence of the Nb<sub>2</sub>CT<sub>x</sub> ASEI on the Li–In alloy anode facilitates the migration of Li and leads to the uniform electrodeposition of Li on the Li–In alloy anode surface.

### 3.4 Electrochemical properties and Li deposition morphology of the Nb<sub>2</sub>CT<sub>x</sub> Li–In alloy anode

The Li deposition and migration processes on the bare Li anode and on the Nb<sub>2</sub>CT<sub>x</sub> Li–In alloy anode are schematically illustrated in Fig. 4a. As indicated, when only Li is employed as an anode material, the formation of the SEI and Li dendrites takes place continuously due to unstable Li electrodeposition and aggregation of the deposited Li. Repeated processes therefore result in Li and electrolyte consumption, ultimately leading to a short cycle life. In contrast, the Nb<sub>2</sub>CT<sub>x</sub>-coated Li–In alloy anodes exhibit a high Li affinity and support proper Li migration, which induces the stable electrodeposition of Li. As a result, the dendritic formation of Li and the exhaustion of active materials can be suppressed. The Nb<sub>2</sub>CT<sub>x</sub> ASEI controls the initial nucleation and growth processes at the interface between the electrolyte and anode. More specifically, the initial electrodeposited Li is intercalated into the layered structure of the Nb<sub>2</sub>CT<sub>x</sub> ASEI and so is protected from any side reactions. Simultaneously, the Li–In anode also induces a uniform and dense Li electrodeposition process because of its strong binding energy to Li and its lower binding energy with the second and third adsorbed Li species compared to the first adsorbed Li. The large Li diffusion barrier of the Li–In anode hinders the local accumulation of the deposited Li. Consequently, the ASEI and Li–In anodes promote reversible electrochemical reactions and improve the cycling performance. Optical images of the Nb<sub>2</sub>CT<sub>x</sub> Cu and Nb<sub>2</sub>CT<sub>x</sub> Li–In anodes are presented in Fig. S8a and b.† In the SEM images (Fig. S8c†), the morphologies of the Nb<sub>2</sub>CT<sub>x</sub> Li–In anodes were similar to those of Nb<sub>2</sub>CT<sub>x</sub> particles because the Nb<sub>2</sub>CT<sub>x</sub> ASEIs were prepared by the LBS method (see Section 2.3). Thus, the Nb<sub>2</sub>CT<sub>x</sub> ASEIs were placed on the Li–In foil without deformations. In addition, we have measured the XRD of the Nb<sub>2</sub>CT<sub>x</sub> ASEI on the Li–In anode to confirm its crystal structure (Fig. S9†). The XRD profile of Nb<sub>2</sub>CT<sub>x</sub> Li–In showed a combination of Li–In anode shown in Fig. 1a and Nb<sub>2</sub>CT<sub>x</sub> shown in Fig. S6.† Although the Nb<sub>2</sub>CT<sub>x</sub> ASEI covered the surface of the Li–In anode, the Li–In signals appear due to the penetration depth of X-rays. Based on the XRD profiles of the Nb<sub>2</sub>CT<sub>x</sub> Li–In anode, the crystal structure of the Nb<sub>2</sub>CT<sub>x</sub> ASEI and Li–In anode exhibited no structural deformation during the LBS process and after the ASEI transfer. Hence, the structures of the Nb<sub>2</sub>CT<sub>x</sub> ASEI and Li–In anode (Fig. S9†), verified *via* XRD, were preserved.

The Li nucleation overpotential ( $\mu_n$ ) is a critical parameter in determining the interfacial energy and the lithium affinity for Li nucleation and growth between the substrate and the Li metal.<sup>16</sup> As the electrodeposition morphology of Li is derived from the initial nuclei and the early growth of Li,<sup>3</sup> a comparison of  $\mu_n$  can be used to evaluate the Li electrodeposition properties of the ASEI. In Fig. 4b,  $\mu_n$  was obtained from the difference in the tip potential ( $\mu_t$ , red circles) and the mass transfer-controlled potential ( $\mu_m$ ),<sup>58</sup> wherein  $\mu_n$  was measured using Cu Nb<sub>2</sub>CT<sub>x</sub>–[Nb<sub>2</sub>CT<sub>x</sub> Li–In asymmetric cells with different thicknesses of the Nb<sub>2</sub>CT<sub>x</sub> ASEI at a constant current density of 0.05 mA cm<sup>–2</sup>. The voltage profiles and measured  $\mu_n$  values are shown in Fig. 4b, and it can be seen that the Nb<sub>2</sub>CT<sub>x</sub> ASEI leads to a reasonable decrease in  $\mu_n$ . The calculated  $\mu_n$  results are presented in Fig. 4c and were determined to be 36.09, 17.69, 15.73, 15.10, and 13.59 mV for the 0.00, 2.02, 4.21, 7.68, and 10.12  $\mu\text{m}$ -thick ASEI layers, respectively. These results indicate that  $\mu_n$  converged when the thickness of the ASEI was increased. Thus, the favorable Li affinity and low Li diffusion barrier of Nb<sub>2</sub>CT<sub>x</sub> provide a suitable substrate for Li nucleation and growth. Upon consideration of the Li nucleation behavior, in addition to the gravimetric and volumetric energy densities, a thickness of 4.21  $\mu\text{m}$  was considered to be the most suitable for the Nb<sub>2</sub>CT<sub>x</sub> Langmuir–Blodgett ASEI (LBASEI).

To confirm the capacity of the Nb<sub>2</sub>CT<sub>x</sub> Li–In alloy anode, the practical areal capacity was measured again using a symmetric cell (Fig. S10†). The practical areal capacities of the Nb<sub>2</sub>CT<sub>x</sub> Li–In alloy anode were therefore determined to be 39.63 mA h cm<sup>–2</sup> (2926.64 mA h g<sup>–1</sup>), which is acceptable in comparison to that of the pure Li. The inset graph of Fig. S10† shows an expanded voltage profile from 0 to 1 mA h cm<sup>–2</sup>, wherein the height of the initial voltage spike represents the Li affinity of the electrode and follows the same trend as that discussed above.

The SEM images showing the surface morphology of the Nb<sub>2</sub>CT<sub>x</sub> Li–In alloy anode were then examined to understand the features of Li electrodeposited on the surface during the Li electrodeposition process. Fig. 4d–g present the surface morphologies at different Li electrodeposition capacities (1–4 mA h cm<sup>–2</sup>) and at a fixed current density of 1 mA cm<sup>–2</sup> for the Nb<sub>2</sub>CT<sub>x</sub> Li–In anode. In Fig. 4d, the non-uniform particles appearing in a relatively light color belong to the Nb<sub>2</sub>CT<sub>x</sub> ASEI, which is covered by large and flat islands of Li shown in a relatively dark color. As the capacity of the electrodeposited Li increases (Fig. 4e–g), the Nb<sub>2</sub>CT<sub>x</sub> ASEI is covered more completely with Li. As indicated in Fig. 4g, the surface of Li deposited on the Nb<sub>2</sub>CT<sub>x</sub> Li–In anode was smoother and more uniform than those on the Li and Li–In alloy anodes (see also Fig. S11a and b†). These differences are attributed to the high Li affinity, small Li diffusion barrier, and small Li nucleation overpotential of the Nb<sub>2</sub>CT<sub>x</sub> ASEI achieved in the previous results. Cross-sectional images corresponding to the 4 mA h cm<sup>–2</sup> Li re-deposition were observed using the FIB milling technique and EDX elemental mapping of Nb L and In L peaks in the same area (Fig. 4h). In the SEM secondary electron (SE) mode image (Fig. 4h, left), stable Li electrodeposition was observed without pore formation taking place.

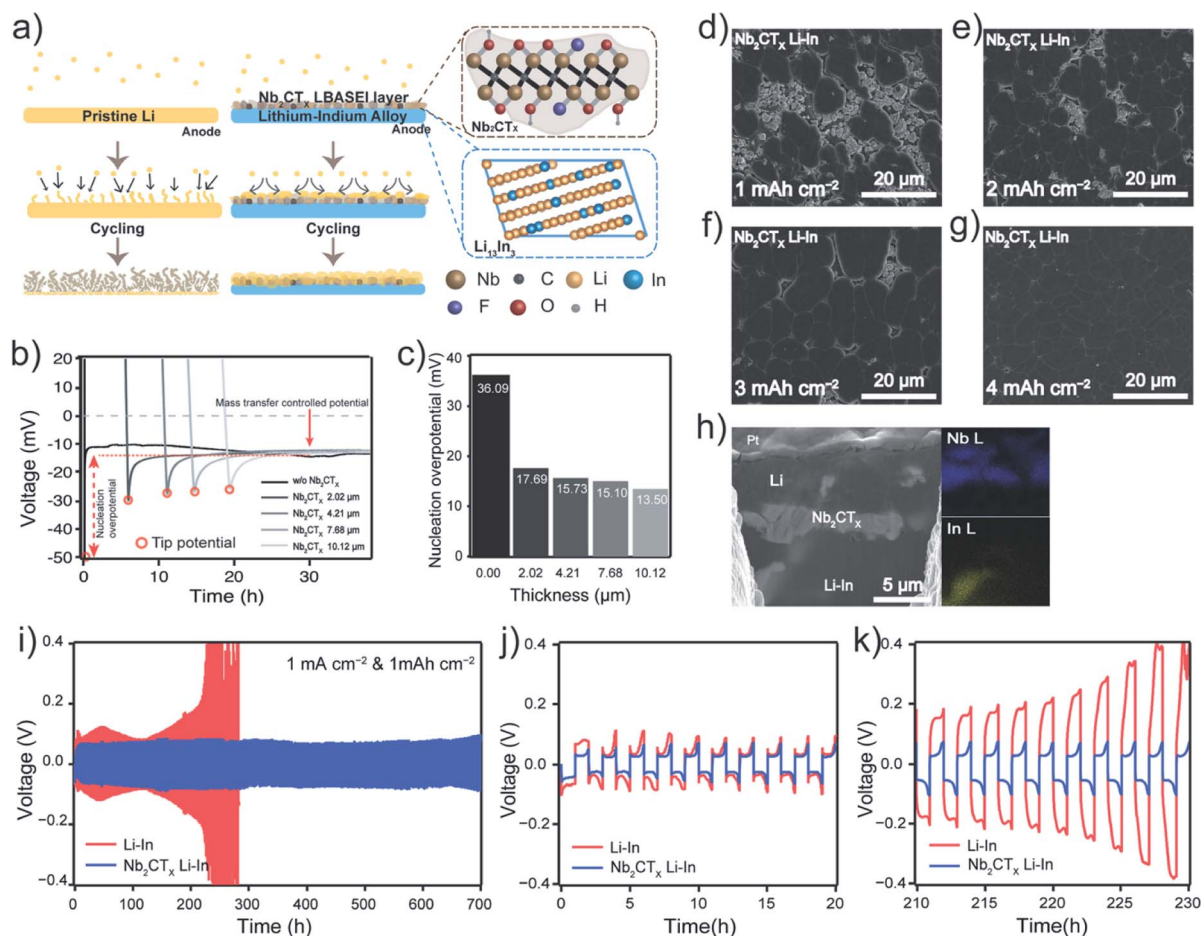


Fig. 4 (a) Schematic illustration for the Li deposition and migration processes occurring at the Nb<sub>2</sub>CT<sub>x</sub> Li-In alloy anode. (b) Galvanostatic voltage profiles of Li deposition based on different thicknesses (black to gray) of the Nb<sub>2</sub>CT<sub>x</sub> LBASEI using a Cu|Nb<sub>2</sub>CT<sub>x</sub> ASEI|Nb<sub>2</sub>CT<sub>x</sub> Li-In asymmetric cell at the same current density of 0.05 mA h cm<sup>-2</sup>. The nucleation overpotentials of Nb<sub>2</sub>CT<sub>x</sub> LBASEI were measured from the voltage difference between the tip potential (red circles) and the mass transfer-controlled potential. (c) The Li nucleation overpotentials were measured with different thicknesses of Nb<sub>2</sub>CT<sub>x</sub> LBASEI, ranging from 0.000 to 10.118 μm. The result obtained for the 0.000 μm sample was measured using the cell with only pure Cu and Li as electrodes. SEM surface morphology micrographs of galvanostatic Li re-deposition onto the Nb<sub>2</sub>CT<sub>x</sub> Li-In at a fixed current density of 1 mA h cm<sup>-2</sup> and different capacities of (d) 1 mA h cm<sup>-2</sup>, (e) 2 mA h cm<sup>-2</sup>, (f) 3 mA h cm<sup>-2</sup>, and (g) 4 mA h cm<sup>-2</sup>. The Li deposition morphologies of Nb<sub>2</sub>CT<sub>x</sub> Li-In were observed for the Li-In|Nb<sub>2</sub>CT<sub>x</sub>|Nb<sub>2</sub>CT<sub>x</sub> Li-In symmetric cell. (h) Cross-sectional FIB image for the 4 mA h cm<sup>-2</sup> Li deposited Nb<sub>2</sub>CT<sub>x</sub> Li-In (right). The bright area at the top of the image is the Pt coating layer for FIB milling, while the dark area in the middle is deposited Li, the bright area in the middle is Nb<sub>2</sub>CT<sub>x</sub> LBASEI, and in the lower area, the bright Li<sub>13</sub>In<sub>3</sub> area and the dark Li can be seen together. Corresponding EDX elemental mapping images for Nb L (right-top) and In L (right-bottom). (i) Galvanostatic Li stripping/plating voltage profiles for Li-In (red) and Nb<sub>2</sub>CT<sub>x</sub> Li-In (blue). The voltage profiles were measured using Li-In|Li-In and Li-In|Nb<sub>2</sub>CT<sub>x</sub>|Nb<sub>2</sub>CT<sub>x</sub> Li-In symmetric cells at a fixed current density of 1 mA cm<sup>-2</sup> and capacity of 1 mA h cm<sup>-2</sup>. (j) The enlarged voltage profiles of (i) from 0 to 20 h. (k) Similarly, the enlarged profiles from 210 to 230 h.

Galvanostatic stripping/plating cycling was then performed to verify the reversibility of the Nb<sub>2</sub>CT<sub>x</sub> Li-In alloy anodes during repetitive electrochemical reactions. The voltage profiles of the Li-In (red) and Nb<sub>2</sub>CT<sub>x</sub> ASEI Li-In (blue) anodes shown in Fig. 4i were compared under the same conditions. The Li-In symmetric cell showed a sudden voltage spike after 250 h and exhibited relatively wide voltage profiles over the entire range. A high voltage response and a short operating time indicate that a relatively more irreversible electrochemical reaction occurred on the Li-In alloy anode. This is because the revealed Li<sub>13</sub>In<sub>3</sub> porous clusters after Li stripping and electrodeposited Li during the charging process are not protected by the ASEI, causing irregular electrodeposition and parasitic reaction during long-

term cycling. In contrast, the Nb<sub>2</sub>CT<sub>x</sub> Li-In alloy anode showed a narrow voltage curve for >700 h, indicating that the stability of Li stripping/plating was improved. The almost identical voltage peaks compared to the initial stage confirm that the formation of an SEI was suppressed, as was the irreversible electrochemical reaction. The enlarged voltage profiles are shown in Fig. 4j and k. As indicated, the Nb<sub>2</sub>CT<sub>x</sub> Li-In alloy anodes exhibit the same shape and magnitude of the profiles in every cycle. However, the Li-In alloy anode (red) shows relatively unstable voltage curves and large voltage spikes over 0–20 h. After 200 h, the Li-In alloy anode shows a noticeable increase in the voltage spikes. These are common features of SEI evolution and electrolyte degradation. To investigate the electrochemical

effect of the  $\text{Nb}_2\text{CT}_x$  ASEI, the voltage profiles of the Li–In and  $\text{Nb}_2\text{CT}_x$  Li–In alloy anodes were compared (Fig. 4i–k and S12a†). Additionally, the same experiment was conducted using the Li–In and  $\text{Nb}_2\text{CT}_x$  Li–In symmetric cells at a higher current density ( $2 \text{ mA cm}^{-2}$ ) and capacity ( $2 \text{ mA h cm}^{-2}$ ) (Fig. S12b†). Both electrodes showed reduced lifetimes and broad voltage responses; however, the overall trends were comparable.

### 3.5 Full cell performance of the $\text{Nb}_2\text{CT}_x$ Li–In alloy anode paired with NCM811

Full cell cycling was then performed to evaluate the battery cycle life and reversibility. The full cells were fabricated with an NCM811 cathode ( $4.1 \text{ mA h cm}^{-2}$ ), and the corresponding n/p ratios of Li, Li–In, and  $\text{Nb}_2\text{CT}_x$  Li–In in the full cells were 11.10, 9.76, and 9.65, respectively. The n/p ratio was calculated from the practical areal capacity (Fig. 1b and S9†) and refers to the amount of excess Li for the cathode capacity. The amount of

electrolyte used in all the coin cells was  $8.6 \mu\text{L (mA h)}^{-1}$ . Cycling was performed at 0.5C ( $2.05 \text{ mA cm}^{-2}$ ) for charging and 1.0C ( $4.1 \text{ mA cm}^{-2}$ ) for discharging (Fig. 5a). The battery life was determined as 80% of the initial discharge capacity (yellow dashed line in Fig. 5a), excluding the formation step. Full cells containing Li and Li–In alloy anodes exhibited cycle lives of approximately 80 and 140 cycles, while the  $\text{Nb}_2\text{CT}_x$  Li–In alloy anode maintained a capacity and a coulombic efficiency (CE) of >99.7% over 250 cycles. These results demonstrated that the local growth of Li dendrites and any parasitic side reactions were effectively controlled using the  $\text{Nb}_2\text{CT}_x$  Li–In alloy anode. For a detailed analysis of full cell cycling, the corresponding charge/discharge voltage profiles of the Li, Li–In, and  $\text{Nb}_2\text{CT}_x$  Li–In alloy anodes were obtained (Fig. 5b–d). The major components of the voltage profile are as follows: (1) the starting voltage of charge and discharge, (2) the change in the voltage slope in the galvanostatic region, (3) the starting point and length of constant voltage charging, and (4) the final capacity of

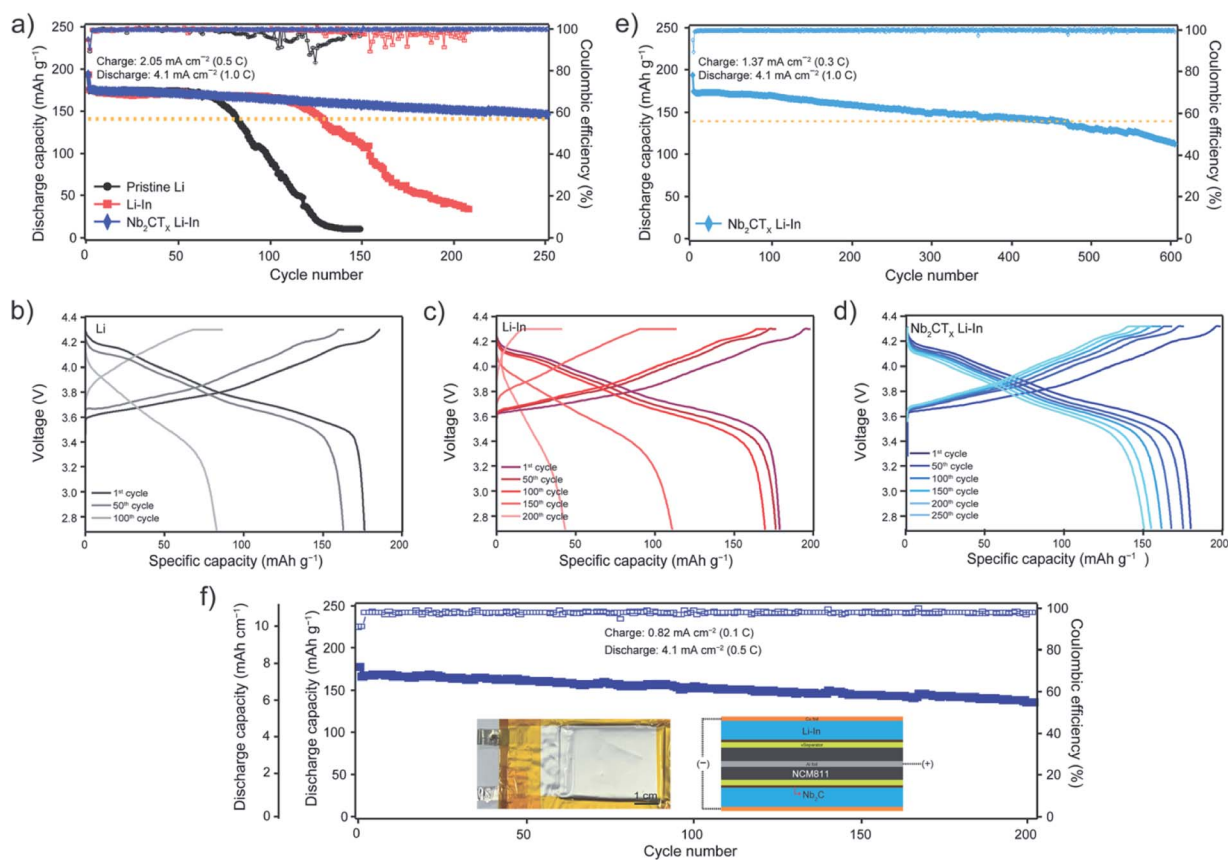


**Fig. 5** Electrochemical full-cell cycling performance with  $\text{Nb}_2\text{CT}_x$  Li–In. (a) Cycling performances of Li|NCM811 (black), Li–In|NCM811 (red), and Li–In  $\text{Nb}_2\text{CT}_x$ |NCM811 (blue) based on the discharge capacity (filled symbols, left axis) and the coulombic efficiency (empty symbols, right axis). The operating conditions of full-cell cycling were 0.5C for charging, 1.0C for discharging, and a voltage window of 2.7–4.3 V. The first highest discharge capacity point was measured in the formation cycle (0.1C charge & discharge) and the yellow dashed line indicates 80% of the initial discharge capacity for each cell. Corresponding voltage profiles for (b) Li|NCM811, (c) Li–In|NCM811, and (d) Li–In  $\text{Nb}_2\text{CT}_x$ |NCM811. (e) Cycling performance of Li–In  $\text{Nb}_2\text{CT}_x$ |NCM811 based on the discharge capacity (filled symbols, left axis) and the coulombic efficiency (empty symbols, right axis) with 0.3C for charging, 1C for discharging, and a voltage window of 2.7–4.3 V. The first highest discharge capacity point was measured in the formation cycle (0.1C charge & discharge) and the yellow dashed line indicates 80% of the initial discharge capacity of the Li–In  $\text{Nb}_2\text{CT}_x$ |NCM811 full-cell. (f) Cycling performance based on the gravimetric and areal discharge capacities (filled symbols) and the coulombic efficiencies (open symbols) for the Li–In  $\text{Nb}_2\text{CT}_x$ |NCM811 pouch cell at 0.1C charge and 0.5C discharge with a voltage window of 2.7–4.3 V. The insets present a photographic image of the pouch cell and a schematic representation of its stacking configuration.

each process. Components (1) and (2) reflect the influence of the impedance components accumulated by repeated cycling, while components (3) and (4) represent cell degradation as a result of (1) and (2). As shown, the Li and Li–In alloy anodes exhibited massive changes after approximately 80 and 125 cycles, respectively. However, the Nb<sub>2</sub>CT<sub>x</sub> Li–In alloy anode (Fig. 5d) showed only a small change compared to the other systems. This is consistent with the results of previous analyses of electrochemical reversibility based on the Li binding energy, Li diffusion properties, and physical morphology, and confirms that the designed anode is suitable for application in full-cell electrochemical systems. To investigate the electrochemical effect of Li–In on the Nb<sub>2</sub>CT<sub>x</sub> ASEI, we performed an additional experiment with Nb<sub>2</sub>CT<sub>x</sub> Li and Nb<sub>2</sub>CT<sub>x</sub> Li–In anodes. Although Li prefers to deposit on the Nb<sub>2</sub>CT<sub>x</sub> ASEI, the CE of any metallic anode, including both Li and Li–In, is not 100%; thus, the active Li must be consumed during cycling. Li consumption during each cycle will eventually lead to the exposure of intermetallic Li–In, in which the exposed intermetallic phase helps to stabilize the Li electrodeposition and improve the reversibility of Li plating/stripping. (2) Based on our DFT analyses, the diffusion barrier of Nb<sub>2</sub>CT<sub>x</sub> was 0.021 eV, which enables Li diffusion at room temperature (Fig. 3h). (3) The comparison between Fig. 2 and 3h shows that Li<sub>13</sub>In<sub>3</sub> has a stronger Li affinity than Nb<sub>2</sub>CT<sub>x</sub>, demonstrating more uniform Li deposition on the intermetallic Li–In. (4) MXene materials have electrical conductivity as high as that of metals. When these materials are used as ASEIs, Li is directly electrodeposited on the surfaces. However, Nb-based MXenes have a relatively low electrical conductivity.<sup>32,56</sup> According to previous studies, Nb<sub>2</sub>CT<sub>x</sub> exhibits a resistance about 100 times higher than that of conventional Ti<sub>2</sub>C at room temperature. This suggests that Li electrodeposition starts at the surface of the Li–In anode, and proliferates through the surfaces of the Nb<sub>2</sub>CT<sub>x</sub> ASEI (please see Fig. 4d–h). The better controlled Li electrodeposition in the presence of the Nb<sub>2</sub>CT<sub>x</sub> ASEI stabilizes the overall electrochemical reversibility of the Nb<sub>2</sub>CT<sub>x</sub> Li–In anode. As shown in Fig. S13† and 5a, the Nb<sub>2</sub>CT<sub>x</sub> Li–In anode exhibited a longer cycle life under the same conditions. Thus, based on the aforementioned reasons and experimental results, the Li–In anode with the Nb<sub>2</sub>CT<sub>x</sub> ASEI stabilizes Li electro-deposition/dissolution, thus promoting higher electrochemical reversibility. Based on these results, the Li–In anode provides sufficient improvement for Li electro-deposition/dissolution under the Nb<sub>2</sub>CT<sub>x</sub> ASEI.

The Nyquist plot shown in Fig. S14† shows the impedance results after the 5<sup>th</sup>, 10<sup>th</sup>, and 15<sup>th</sup> cycles. Compared to the other full cells, the full cell containing the Nb<sub>2</sub>CT<sub>x</sub> Li–In alloy anode exhibited small changes after cycling. This is in agreement with the previous results of the electrochemical performance, which is further evidence that the designed anode can suppress the formation of internal impedance.

Fig. 5e shows the cycling performance under charging at 0.3C (1.23 mA cm<sup>-2</sup>) and discharge at 1.0C (4.1 mA cm<sup>-2</sup>). The cycling performance of the Nb<sub>2</sub>CT<sub>x</sub> Li–In alloy anode was maintained at >80% of the discharge capacity compared to the initial capacity until after 450 cycles, beyond which it continued to show a stable capacity retention rate and CE.

Finally, pouch cells based on Nb<sub>2</sub>CT<sub>x</sub> Li–In alloy anodes and NCM811 cathodes were fabricated with an energy density of ~272 W h kg<sup>-1</sup> and ~500 W h L<sup>-1</sup>. The pouch cell cycling performance is presented in Fig. 5f, while a photographic image of the pouch cell and a schematic representation of the stacking configuration are shown in the insets. The pouch cell was designed with a 8.2 mA h cm<sup>-2</sup> cathode (double-sided cathode), an n/p ratio of 9.65, and a limited electrolyte amount of 2.4 μL (mA h)<sup>-1</sup>, and the process was performed at 0.1C (0.82 mA cm<sup>-2</sup>) for charging and 0.5C (4.1 mA cm<sup>-2</sup>) for discharging. As indicated, stable cycling was maintained for >200 cycles. This result represents a consistent performance, and demonstrates the good reversibility of our designed anode.

## 4. Conclusions

In this study, we designed a new anode that benefited from the characteristics of each component for lithium–metal battery systems with a Li–In alloy anode and a Nb<sub>2</sub>CT<sub>x</sub> Langmuir–Blodgett artificial solid-electrolyte interface (LBA-SEI). Our strategy was based on the assumption that the Li–In alloy anode and the Nb<sub>2</sub>CT<sub>x</sub> ASEI complement each other and maximize the anode performance. The mechanism of adsorption and diffusion to ensure reversibility at the anode interface was investigated using computational and physico-chemical approaches. We found that the large Li affinity and Li diffusion barrier of Li<sub>13</sub>In<sub>3</sub> led to uniform Li electrodeposition. In addition, the suitable Li binding energy, low diffusion barrier, and quasi-hosting feature of the Nb<sub>2</sub>CT<sub>x</sub> ASEI effectively protected the surface of the Li–In alloy anode. The full cell cycling performance of the Nb<sub>2</sub>CT<sub>x</sub> Li–In alloy anode was evaluated using a high loading NCM811 cathode (4.1 mA h cm<sup>-2</sup>), and the discharge capacity was stably maintained until after 450 cycles. Furthermore, we verified the extension of the cycle performance over >200 cycles in a pouch cell system (*i.e.*, ~272 W h kg<sup>-1</sup>, 500 W h L<sup>-1</sup>) paired with a practical NCM811 cathode and the lowest electrolyte amount of 2.4 μL (mA h)<sup>-1</sup>. To make this system suitable for application in commercial products, it will be necessary to increase its scale, reduce the n/p ratio, and optimize the cathode; however, our results confirm optimization of a suitable anode design, which is the most critical ongoing issue in the Li–metal battery industry.

## Author contributions

S. H. L., M. S. K. and W. I. C. conceptualized and investigated the overall study. M. S. K., W. I. C. and W. K. supervised the overall research and reviewed the writing. W. I. C. contributed to the funding acquisition. J.-H. L. performed and supervised the first-principles calculations for Li–In and Nb<sub>2</sub>CT<sub>x</sub>. J.-H. R. contributed to the material synthesis. J.-H. R., V. D. and B. G. L. investigated the material characteristics. S. H. L. performed all the experiments, characterization and analysis and wrote the manuscript. All the authors discussed the manuscript and provided comments.

## Conflicts of interest

There are no conflicts to declare.

## Acknowledgements

We thank Kwang-Ryeol Lee at KIST for helpful discussions. This work was supported by the Korea Institute of Science and Technology Institutional Program (project no. 2E31873) and the project for Development of Technology for Materials and Components (project no. 20016022) funded by the Ministry of Trade, Industry & Energy (MOTIE, Korea). JHL was supported by the Korea Institute of Science and Technology Institutional Program (project no. 2E31201). Computational resources provided by the KISTI Supercomputing Centre (project no. KSC-2020-CRE-0361) are gratefully acknowledged.

## Notes and references

- F. Duffner, N. Kronemeyer, J. Tübke, J. Leker, M. Winter and R. Schmich, *Nat. Energy*, 2021, **6**, 123–134.
- J. Liu, Z. Bao, Y. Cui, E. J. Dufek, J. B. Goodenough, P. Khalifah, Q. Li, B. Y. Liaw, P. Liu, A. Manthiram, Y. S. Meng, V. R. Subramanian, M. F. Toney, V. V. Viswanathan, M. S. Whittingham, J. Xiao, W. Xu, J. Yang, X.-Q. Yang and J.-G. Zhang, *Nat. Energy*, 2019, **4**, 180–186.
- X. R. Chen, B. C. Zhao, C. Yan and Q. Zhang, *Adv. Mater.*, 2021, **33**, 1–23.
- S. H. Park, D. Jun, G. H. Lee, S. G. Lee and Y. J. Lee, *J. Mater. Chem. A*, 2021, 14656–14681.
- R. Xu, X. B. Cheng, C. Yan, X. Q. Zhang, Y. Xiao, C. Z. Zhao, J. Q. Huang and Q. Zhang, *Mater.*, 2019, **1**, 317–344.
- J. Zheng, M. S. Kim, Z. Tu, S. Choudhury, T. Tang and L. A. Archer, *Chem. Soc. Rev.*, 2020, **49**, 2701–2750.
- R. Zhang, N. W. Li, X. B. Cheng, Y. X. Yin, Q. Zhang and Y. G. Guo, *Adv. Sci.*, 2017, **4**, 1600445.
- S. Wei, Z. Cheng, P. Nath, M. D. Tikekar, G. Li and L. A. Archer, *Sci. Adv.*, 2018, **4**, 1–9.
- C. Fang, X. Wang and Y. S. Meng, *Trends Chem.*, 2019, **1**, 152–158.
- J. Xie, J. Wang, H. R. Lee, K. Yan, Y. Li, F. Shi, W. Huang, A. Pei, G. Chen, R. Subbaraman, J. Christensen and Y. Cui, *Sci. Adv.*, 2018, **4**, 2–10.
- Y. Gao, Z. Yan, J. L. Gray, X. He, D. Wang, T. Chen, Q. Huang, Y. C. Li, H. Wang, S. H. Kim, T. E. Mallouk and D. Wang, *Nat. Mater.*, 2019, **18**, 384–389.
- Y. Han, B. Liu, Z. Xiao, W. Zhang, X. Wang, G. Pan, Y. Xia, X. Xia and J. Tu, *InfoMat*, 2021, **3**, 155–174.
- J. Li, Z. Kong, X. Liu, B. Zheng, Q. Hua, E. Garratt, T. Schuelke and K. Wang, *InfoMat*, 2021, 1–31.
- Z. Tu, S. Choudhury, M. J. Zachman, S. Wei, K. Zhang, L. F. Kourkoutis and L. A. Archer, *Nat. Energy*, 2018, **3**, 310–316.
- M. Wan, S. Kang, L. Wang, H. W. Lee, G. W. Zheng, Y. Cui and Y. Sun, *Nat. Commun.*, 2020, **11**, 1–10.
- K. Yan, Z. Lu, H. W. Lee, F. Xiong, P. C. Hsu, Y. Li, J. Zhao, S. Chu and Y. Cui, *Nat. Energy*, 2016, **1**, 16010.
- L. L. Kong, L. Wang, Z. C. Ni, S. Liu, G. R. Li and X. P. Gao, *Adv. Funct. Mater.*, 2019, **29**, 1–10.
- Q. Liu, S. Zhou, C. Tang, Q. Zhai, X. Zhang and R. Wang, *Energies*, 2018, **11**, 1–5.
- S. Chen, X. Yang, J. Zhang, J. Ma, Y. Meng, K. Tao, F. Li and J. Geng, *Electrochim. Acta*, 2021, **368**, 137626.
- X. Liang, Q. Pang, I. R. Kochetkov, M. S. Sempere, H. Huang, X. Sun and L. F. Nazar, *Nat. Energy*, 2017, **6**, 17119.
- A. L. Santhosha, L. Medenbach, J. R. Buchheim and P. Adelhelm, *Batteries Supercaps*, 2019, **2**, 497.
- C. Wu, H. Huang, W. Lu, Z. Wei, X. Ni, F. Sun, P. Qing, Z. Liu, J. Ma, W. Wei, L. Chen, C. Yan and L. Mai, *Adv. Sci.*, 2020, **7**, 1902643.
- Y. Zhou, J. Zhang, K. Zhao, Y. Ma, H. Zhang, D. Song, X. Shi, L. Zhang and Y. Ding, *Energy Storage Mater.*, 2021, **39**, 403–411.
- S. Jin, Y. Ye, Y. Niu, Y. Xu, H. Jin, J. Wang, Z. Sun, A. Cao, X. Wu, Y. Luo, H. Ji and L. J. Wan, *J. Am. Chem. Soc.*, 2020, **142**, 8818–8826.
- M. S. Kim, Deepika, S. H. Lee, M. S. Kim, J.-H. Ryu, K. R. Lee, L. A. Archer and W. Il Cho, *Sci. Adv.*, 2019, **5**, 1–16.
- Z. Han, C. Zhang, Q. Lin, Y. Zhang, Y. Deng, J. Han, D. Wu, F. Kang, Q. H. Yang and W. Lv, *Small Methods*, 2021, **5**, 1–20.
- M. S. Kim, J.-H. Ryu, Deepika, Y. R. Lim, I. W. Nah, K.-R. Lee, L. A. Archer and W. Il Cho, *Nat. Energy*, 2018, **3**, 889–898.
- J. Bobnar, M. Lozinšek, G. Kapun, C. Njél, R. Dedryvère and B. Genorio, *Sci. Rep.*, 2018, **8**, 5819.
- C. Li, Q. Lan, Y. Yang, H. Shao and H. Zhan, *ACS Appl. Mater. Interfaces*, 2019, **11**, 2479–2489.
- B. Han, D. Feng, S. Li, Z. Zhang, Y. Zou, M. Gu, H. Meng, C. Wang, K. Xu, Y. Zhao, H. Zeng, C. Wang and Y. Deng, *Nano Lett.*, 2020, **20**, 4029–4037.
- R. Rojaee and R. Shahbazian-Yassar, *ACS Nano*, 2020, **14**, 2628–2658.
- J. Halim, I. Persson, E. J. Moon, P. Kühne, V. Darakchieva, P. O. Å. Persson, P. Eklund, J. Rosen and M. W. Barsoum, *J. Phys.: Condens. Matter*, 2019, **31**(16), 1–9.
- C. Y. Li, M. W. Barsoum, S. Kim, Y. Zheng, W. Huang, Y. Tu, S. Wang, H. Qi, Q. Pan and S. Kota, *Nanoscale Adv.*, 2018, **1**, 395–402.
- M. Naguib, J. Halim, J. Lu, K. M. Cook, L. Hultman, Y. Gogotsi and M. W. Barsoum, *J. Am. Chem. Soc.*, 2013, **135**, 15966–15969.
- J. Hu, B. Xu, C. Ouyang, Y. Zhang and S. A. Yang, *RSC Adv.*, 2016, **6**, 27467–27474.
- L. Gao, C. Ma, S. Wei, A. V. Kuklin, H. Zhang and H. Ågren, *ACS Nano*, 2021, **15**, 954–965.
- M. S. Kim, L. Ma, S. Choudhury, S. S. Moganty, S. Wei and L. A. Archer, *J. Mater. Chem. A*, 2016, **4**, 14709–14719.
- P. E. Blöchl, *Phys. Rev. B: Condens. Matter Mater. Phys.*, 1994, **50**, 17953–17979.
- D. Joubert, *Phys. Rev. B: Condens. Matter Mater. Phys.*, 1999, **59**, 1758–1775.
- G. Kresse and J. Hafner, *Phys. Rev. B: Condens. Matter Mater. Phys.*, 1993, **47**, 558–561.

- 41 G. Kresse and J. Hafner, *Phys. Rev. B: Condens. Matter Mater. Phys.*, 1994, **49**, 14251–14269.
- 42 J. Kresse and G. Furthmüller, *J. Phys. Chem. A*, 1996, **54**, 11169.
- 43 G. Kresse and J. Furthmüller, *Comput. Mater. Sci.*, 1996, **6**, 15–50.
- 44 I. Hamada, *Phys. Rev. B: Condens. Matter Mater. Phys.*, 2014, **89**, 121103.
- 45 C. Elsässer, M. Fähnle, C. T. Chan and K. M. Ho, *Phys. Rev. B: Condens. Matter Mater. Phys.*, 1994, **49**, 13975–13978.
- 46 J. Stöhr, W. Müller and H. Schäfer, *Z. Naturforsch., B: Anorg. Chem., Org. Chem.*, 1978, **33**, 1434–1437.
- 47 A. G. Marinopoulos, P. Santos and J. Coutinho, *Phys. Rev. B: Condens. Matter Mater. Phys.*, 2015, **92**, 1–11.
- 48 G. Henkelman, B. P. Uberuaga and H. Jónsson, *J. Chem. Phys.*, 2000, **113**, 9901–9904.
- 49 G. Henkelman and H. Jónsson, *J. Chem. Phys.*, 2000, **113**, 9978–9985.
- 50 J. Sangster and A. D. Pelton, *J. Phase Equilib.*, 1991, **12**, 290–292.
- 51 S. A. Webb, L. Baggetto, C. A. Bridges and G. M. Veith, *J. Power Sources*, 2014, **248**, 1105–1117.
- 52 Y. Dong, H. Shi and Z. S. Wu, *Adv. Funct. Mater.*, 2020, **30**, 1–24.
- 53 L. Hu, Y. Sun, S. J. Gong, H. Zong, K. Yu and Z. Zhu, *New J. Chem.*, 2020, **44**, 7902–7911.
- 54 S. Zhao, X. Meng, K. Zhu, F. Du, G. Chen, Y. Wei, Y. Gogotsi and Y. Gao, *Energy Storage Mater.*, 2017, **8**, 42–48.
- 55 J. Halim, K. M. Cook, M. Naguib, P. Eklund, Y. Gogotsi, J. Rosen and M. W. Barsoum, *Appl. Surf. Sci.*, 2016, **362**, 406–417.
- 56 J. Halim, J. Palisaitis, J. Lu, J. Thörnberg, E. J. Moon, M. Precner, P. Eklund, P. O. A. Persson, M. W. Barsoum and J. Rosen, *ACS Appl. Nano Mater.*, 2018, **1**, 2455–2460.
- 57 Y. Xie, M. Naguib, V. N. Mochalin, M. W. Barsoum, Y. Gogotsi, X. Yu, K. W. Nam, X. Q. Yang, A. I. Kolesnikov and P. R. C. Kent, *J. Am. Chem. Soc.*, 2014, **136**, 6385–6394.
- 58 R. Zhang, X.-R. Chen, X. Chen, X.-B. Cheng, X.-Q. Zhang, C. Yan and Q. Zhang, *Angew. Chem., Int. Ed.*, 2017, **56**, 7764–7768.